Electronic Supplementary Material (ESI) for ChemComm.

A Transient Ru^{III} Azide Complex with Metallo-Staudinger Reactivity

Sungho V. Park,[†] Charles G. Fry,[†] Eckhard Bill[‡] and John F. Berry*[,†]

[†]Department of Chemistry, University of Wisconsin – Madison, 1101 University Avenue, Madison, Wisconsin 53706, United States

[‡]Max-Planck-Institut für Chemische Energiekonversion, Stiftstrasse 34-36, D-45470 Mülheim an der Ruhr, Germany

Contents

General Considerations

All operations were conducted air-free using either a Schlenk line or a nitrogen-filled glovebox unless specified otherwise. PPh_3 (99%) was purchased from Sigma and recrystallized from EtOH under N_2. Solvents were distilled with appropriate drying agents (B_2O_3 for d_6-acetone, P_2O_5 for d_3-acetonitrile, and CaH_2 for dichloromethane) and sparged with N_2 prior to use.

The complex $[(Py_5Me_2)Ru^{II}(N_3)](PF_6)$ (**2**) was synthesized according to a literature procedure.[1] The oxidant $[(4\text{-}BrC_6H_4)_3N](SbCl_6)$ was purchased from Sigma-Aldrich and used as received. The oxidant $[(4\text{-}BrC_6H_4)_3N](PF_6)$ was synthesized according to a literature procedure.[2] Triphenyl phosphate (>99.0%) and tris(2,4-pentanedionato)chromium(III) (>98.0%) was purchased from TCI America and used as received.

EPR spectra were obtained on a Bruker Elexsys E 500 EPR spectrometer. A continuous flow liquid helium cryostat (Oxford Instruments ESR 900) and an Oxford Instruments 3120 temperature controller were used to control the acquisition temperature. EPR simulations and double-integration were performed by using esim.SL and eview.SL, respectively (available by email from the author EB, ebill@gwdg.de). The powder pattern for $S = 1/2$ were simulated with anisotropic g values and anisotropic line widths, using Gaussian line shapes.

NMR spectra were acquired using a Bruker Avance III 500 MHz spectrometer. ^{1}H NMR spectra were referenced to residual solvent peaks for CD_2HCN ($\delta = 1.94$ ppm). ^{31}P NMR spectra were referenced to the corresponding ^{1}H NMR spectra using absolute referencing.[3,4] Electrospray ionization (ESI) mass spectrometry data were obtained with a Thermo Q Exactive Plus mass spectrometer. UV/vis spectra were acquired on a StellarNet Miniature BLUE-Wave dip-probe spectrometer.

Quantification Method for ^{31}P NMR Spectra

This procedure was adapted from the literature.[5] In a glovebox, a vial was loaded with 12.1 mg of $Cr(acac)_3$, 2.9 mg of sample and 1.5 mg of $OP(OPh)_3$. To this mixture, CD_3CN was added and the resulting solution was loaded in a screw-cap tube. The T_1 inversion recovery tests typically revealed an optimal null time (d7 value) of 0.4 sec. Quantitative ^{31}P spectra were therefore taken with a d1 value of 4 sec.

Synthesis and characterization of 3

Compound **2** (10.1 mg, 13.8 mmol) and 1.06 equivalents of the oxidant $[(4\text{-}BrC_6H_4)_3N](PF_6)$ (9.2 mg, 15 mmol) were pre-loaded into a Schlenk flask with a stirbar in the glovebox. The flask was wrapped with aluminum foil and immersed in a dry ice-acetone bath. To this flask, 6.7 mL of cold acetone, cooled in the same bath, was added to the solid mixture via cannula and the resulting solution was allowed to stir in the dark at -78 °C for 10 minutes to generate **3**. To this solution was added ~ 50 mL of ether to crash out the product. The resulting purple powder was washed with ~ 30 mL of ether quickly in air for subsequent MALDI-TOF and IR measurements.

Yield could not be determined because of the extreme sensitivity of the compound. However, 100% of the oxidant is consumed, as determined by the disappearance of the absorption band of the oxidant at $\lambda \sim 700$ nm within seconds in the UV/vis spectra, used to monitor the *in situ* formation and subsequent degradation of the compound (Figure S15).

MALDI-TOF (m/z): 545 ($[M - 2\ PF_6 - N_3]^+$). IR (ATR): 2005 [$\nu(N_3)$], 1601, 1468, 1443, 1235, 1067, 1035, 834, 761, 652, 634 cm^{-1}. UV/vis (CH_3COCH_3): λ_{max} (ε) = 551 nm (4.1×10^3 mol^{-1} L cm^{-1}). The compound was crystallized by slow diffusion of pentane into an acetone solution at -78 °C for ~ 2 months, followed by further diffusion at -25 °C for two days. Crystallographic data collection was conducted at 100 K in the dark.

Crystallization of 4

Compound **3** was prepared as described above. The compound was dissolved in acetone at -78 °C in the dark and layered with hexanes. Storage of the crystallization setup at -25 °C for 3.5 weeks gave crystals of **4**. Attempts to deliberately synthesize **4** by reaction of $[(Py_5Me_2)Ru^{II}(Cl)](PF_6)$[1,6] and $AgPF_6$ in refluxing acetone gave ESI-MS data (m/z = 646.0757) and crystallographic data (Figure S14) that supported formation of $[(Py_5Me_2)Ru^{II}(PO_2F_2)]^+$ as the dominant species instead of the desired product.

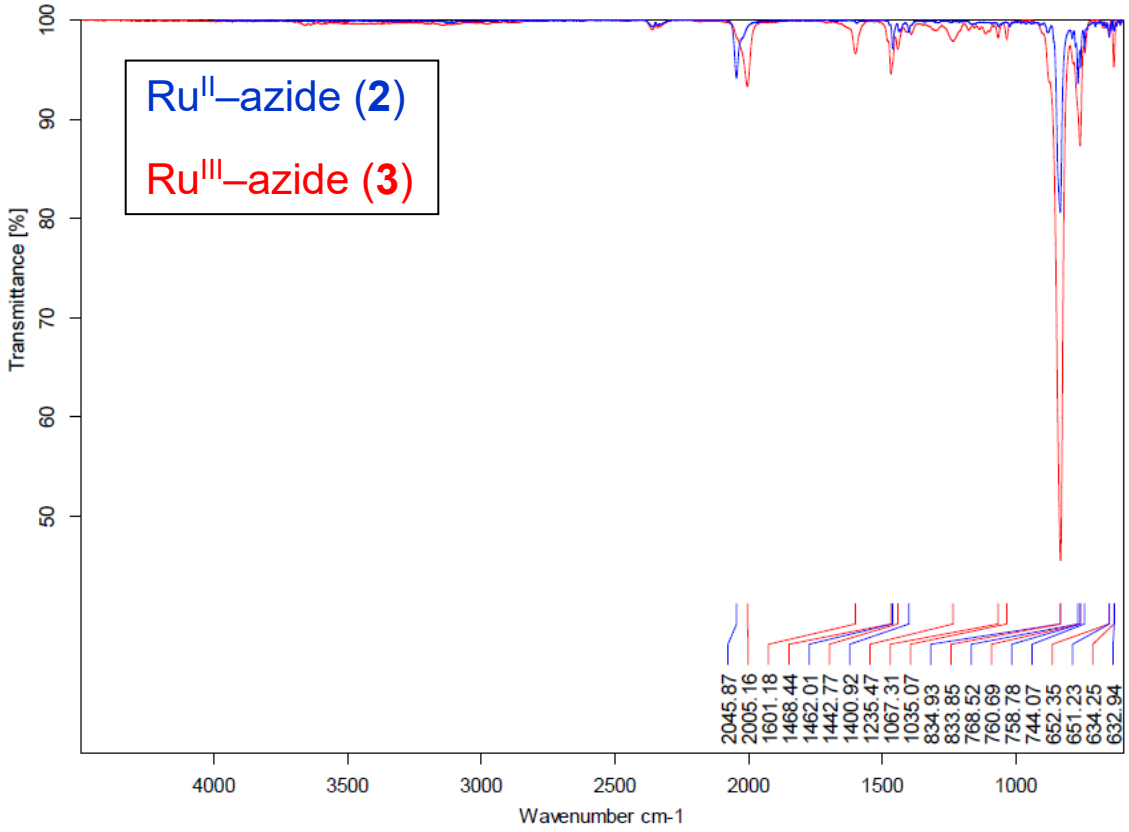

Figure S1. IR spectral comparisons between compounds **2** and **3**.

Reaction of 3 with PPh_3 at -78 °C

Compound **2** (11.9 mg, 16.3 mmol) and 1.00 equivalent of the oxidant $[(4\text{-}BrC_6H_4)_3N](PF_6)$ (10.2 mg, 16.3 mmol) were pre-loaded into a Schlenk flask with a stirbar in the glovebox. The flask was wrapped with aluminum foil and immersed in a dry ice-acetone bath. To this flask, 8 mL of cold acetone, cooled in the same bath, was added to the solid mixture via cannula and the resulting solution was allowed to stir in the dark at -78 °C for 15 minutes to generate **3**. To this solution was added *dropwise* via syringe a solution of 25 equivalents of PPh_3 (106.5 mg, 0.4060 mol) in 7 mL acetone prepared in the glovebox. After three hours of stirring, the reaction mixture was allowed to sit at -78 °C in the dark for an additional 11 hours. To the resulting solution was added ~ 55 mL of dry ether to crash out the product. The precipitate was filtered in air and washed with additional ether. ^{1}H NMR spectroscopic analysis confirmed **2** as the only Ru product. Yield: 79%

Generation of $[(Py_5Me_2)Ru^{II}(N(H)PPh_3)]^{2+}$ (5)

Compound **2** (12.1 mg, 16.5 mmol) and 1.04 equivalents of the oxidant $[(4\text{-}BrC_6H_4)_3N](PF_6)$ (10.8 mg, 17.2 mmol) were pre-loaded into a Schlenk flask with a stirbar in the glovebox. The flask was wrapped with aluminum foil and immersed in a dry ice-acetone bath. To this flask, 9 mL of cold d_6-acetone (containing a small amount of TMS), cooled in the same bath, was added to the solid mixture via cannula and the resulting solution was allowed to stir in the dark at -78 °C for 10 minutes to generate **3**. To this solution was added via syringe a solution of 25 equivalents of PPh_3 (109.8 mg, 0.419 mol) in 3 mL of d_6-acetone prepared in the glovebox. After two hours of stirring, the cold bath was removed and the mixture was allowed to warm to room temperature whereupon the solvent was removed and the residue was washed with ether. The resulting yellow powder contained **5** (11% conversion) which was identified by its characteristic coupling between the NH H atom and the ^{31}P nucleus (Figures S3 & S4) and was quantified using the ^{31}P NMR method described above.

^1H NMR (δ in CD_3CN): 9.09 (d, J = 5.6 Hz, 4H), 2.75 (s, 6H), 2.52 (d, $J_{P\text{-}H}$ = 5.8 Hz, 1H) ppm. The other protons could not be assigned due to heavy overlap of peaks in the aromatic region. ^{31}P NMR (δ in CD_3CN): 42.7 ($J_{P\text{-}H}$ = 5.8 Hz) ppm. ESI-MS: m/z = 411.1085 $[M - 2\ PF_6]^{2+}$. Attempts to deliberately synthesize the phosphinimide complex via alternative routes were unsuccessful.

Other Ru products are compound **2**, compound **4**, and $[(Py_5Me_2)Ru^{II}(CD_3CN)]^{2+}$, which are identified on the basis of the characteristic chemical shifts of their pyridine ortho-H atoms in the Py_5Me_2 ligand (Figure S5). The values are δ = 9.51 ppm and 9.38 ppm for compounds **2** and $[(Py_5Me_2)Ru^{II}(CD_3CN)]^{2+}$, respectively.[1] Formation of compound **4** was supported by its X-ray crystal structure determination from a separate reaction of **3′** with 1.0 equivalent of PPh_3. The pyridine ortho-H atoms of **4** appear at 9.12 ppm.

Other phosphorus products are $[H_2NPPh_3]^+$, $OPPh_3$ and $[Ph_3P{=}N{=}PPh_3]^+$. The ether wash contains $OPPh_3$ with a minor unidentified phosphorus product (δ = 35.4 ppm) in the ^{31}P NMR (Figure S6).

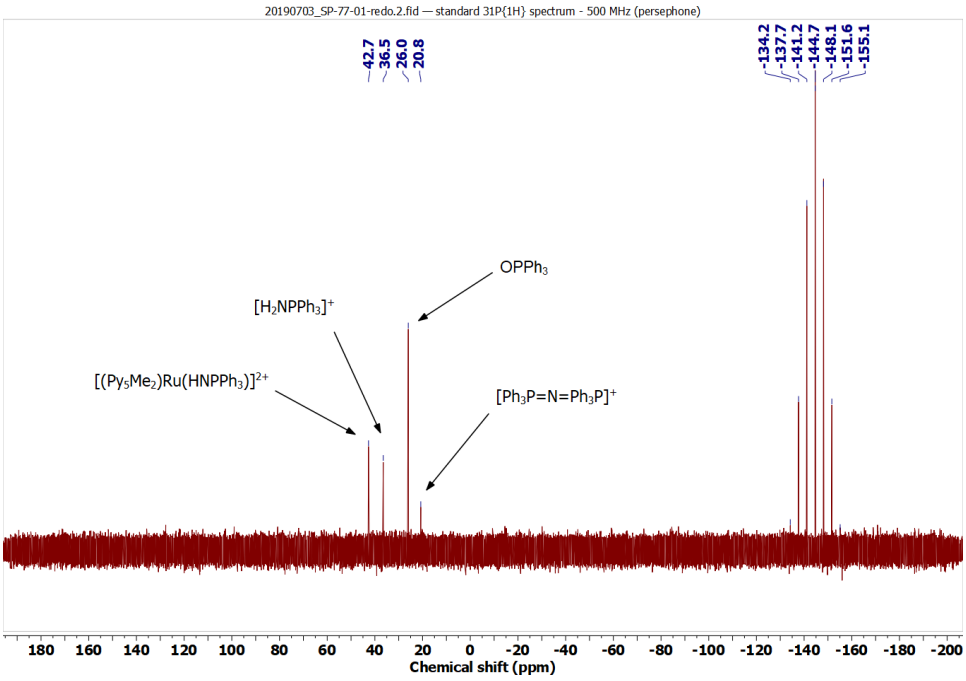

Figure S2. ^{31}P NMR spectrum of the reaction mixture after workup.

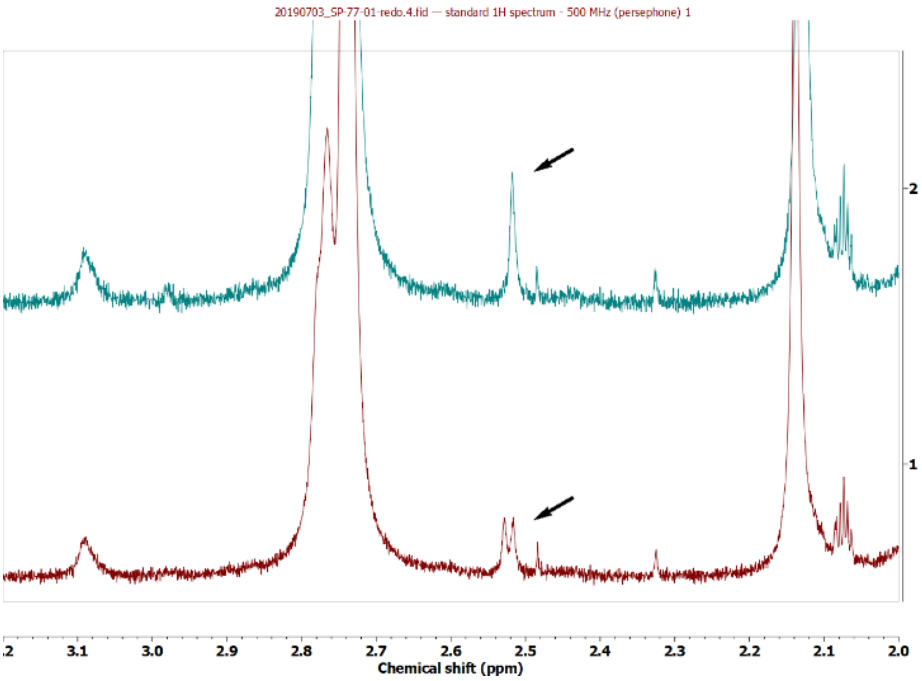

Figure S3. ^{31}P decoupled ^{1}H NMR spectrum (top) shown with the standard ^{1}H (^{31}P coupled) NMR spectrum (bottom). The arrows point to the NH signal of **5**, indicating its splitting due to proximity of the ^{31}P nucleus.

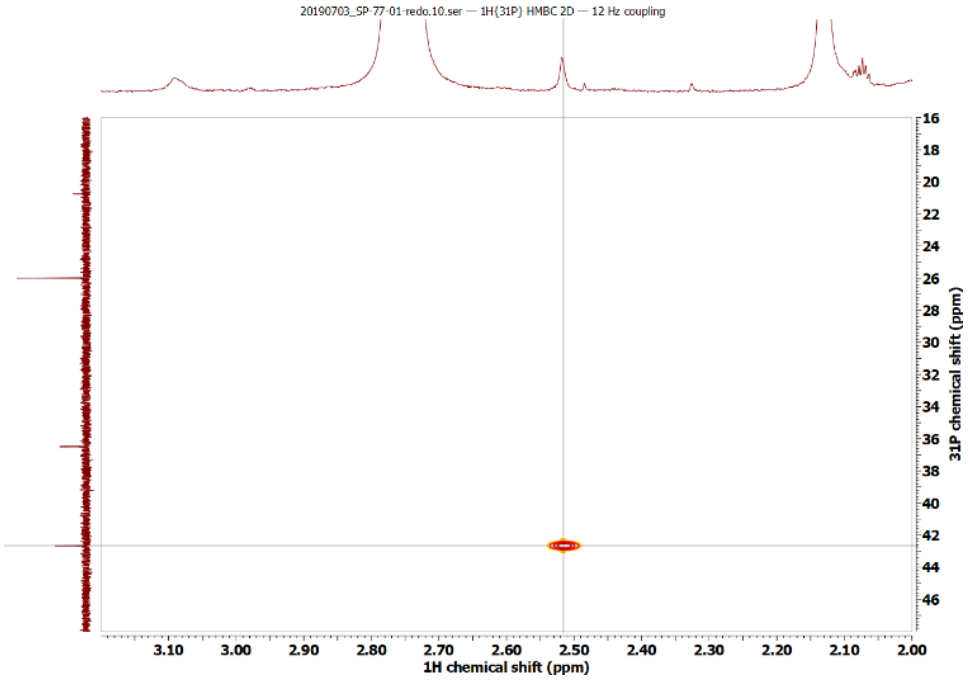

Figure S4. ^{1}H-^{31}P HMBC NMR spectrum of the reaction mixture after workup with cross peak indicating the NH signal and ^{31}P signal of **5**.

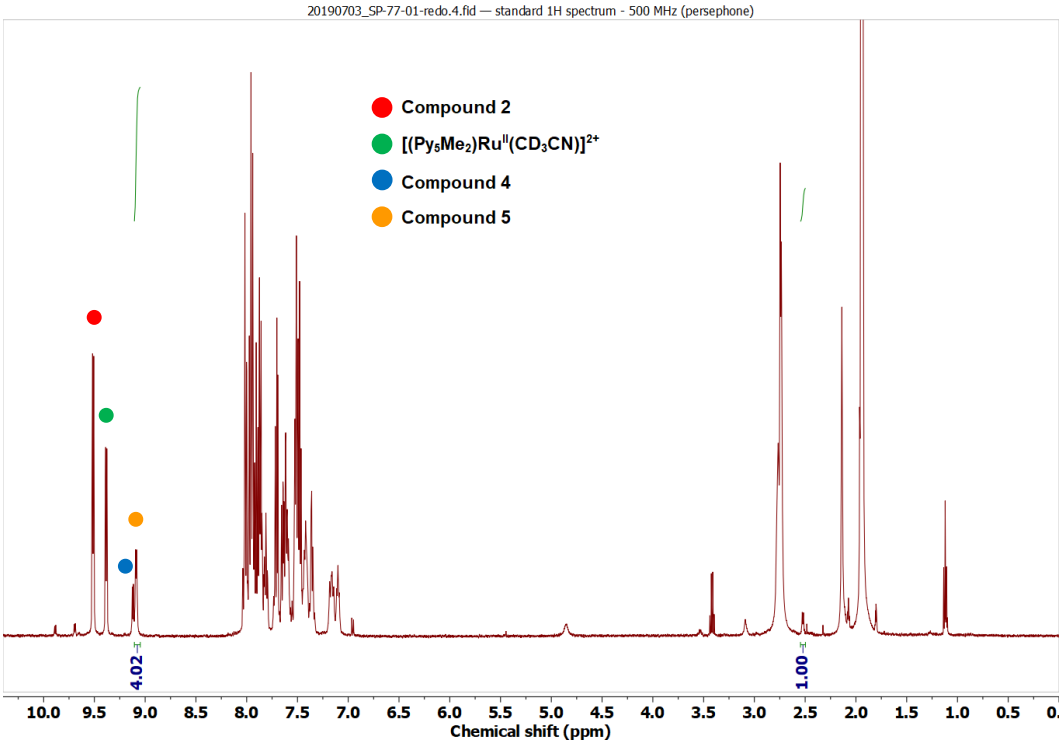

Figure S5. ^{1}H NMR spectrum of the reaction mixture after workup.

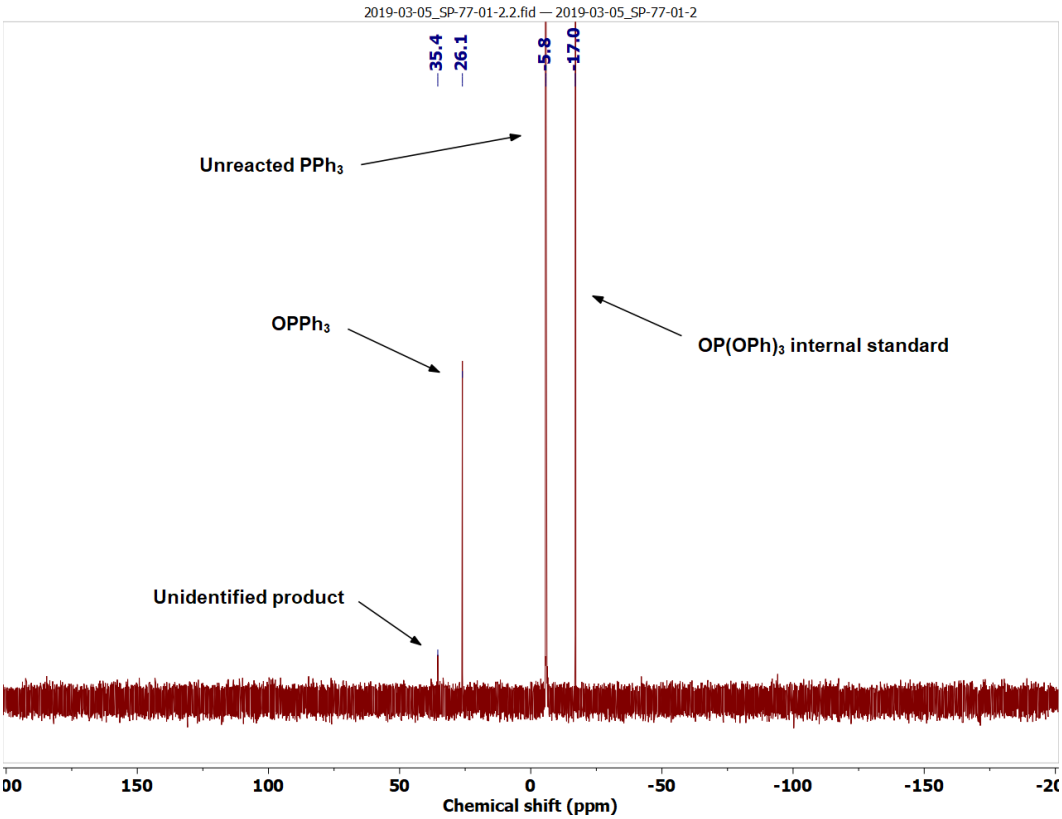

Figure S6. ^{31}P NMR spectrum of the ether wash.

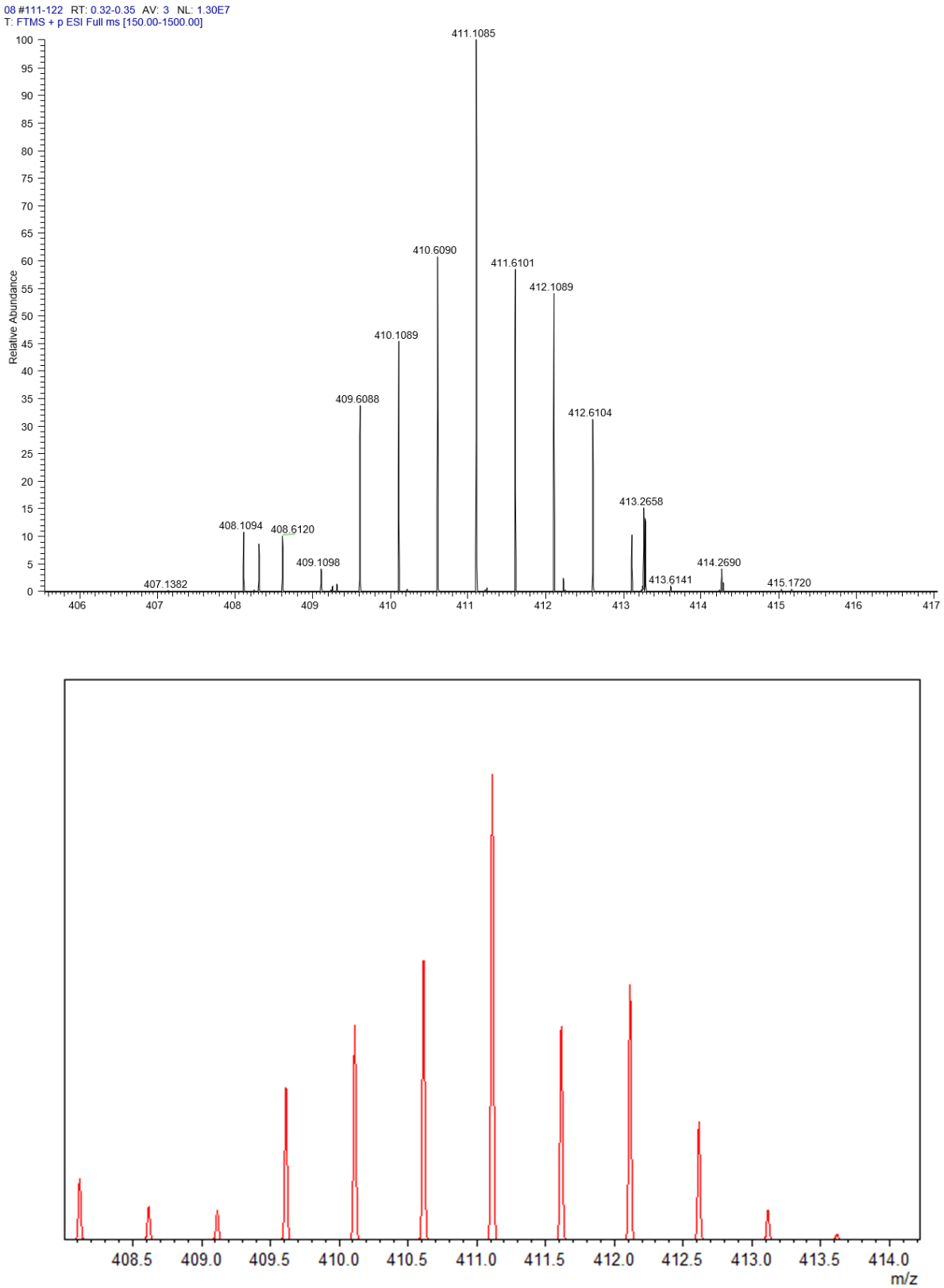

Figure S7. Experimental (top) and simulated (bottom) ESI-MS for **5**. Simulated m/z = 411.1088.

NMR spectrum of the organic layer upon reaction of 3 with 1 equivalent of PPh_3

Compound **5** was generated using the method described above with 1 equivalent of PPh_3 instead of 25 equivalents. The ether wash contains multiple phosphorus products, with a downfield shift in the ^{31}P NMR chemical shifts for $OPPh_3$ and PPh_3, attributable to a proton-mediated equilibrium as described in equation 1.[7] $OPPh_3$ and PPh_3 usually appear at 26.0 ppm and -5.9 ppm; however, here they are observed at 27.3 ppm and -4.6 ppm.

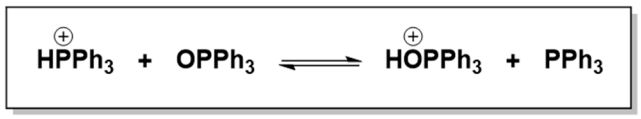

$$\frac{[HPPh_3^+]}{[PPh_3]} = \frac{\delta_{eq} - \delta_{PPh_3}}{\delta_{HPPh_3^+} - \delta_{eq}}$$

(Equation 1)

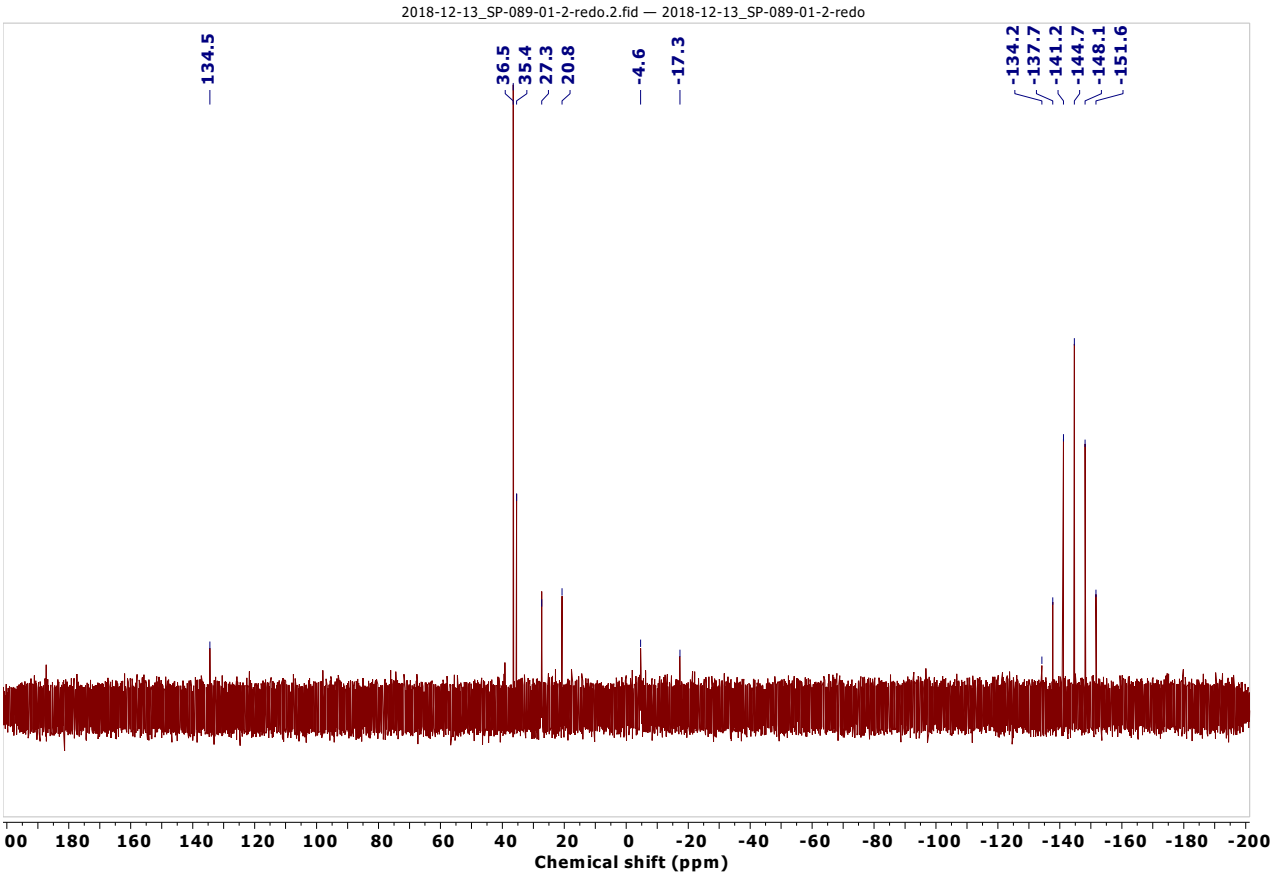

Figure S8. ^{31}P NMR spectrum of the ether wash.

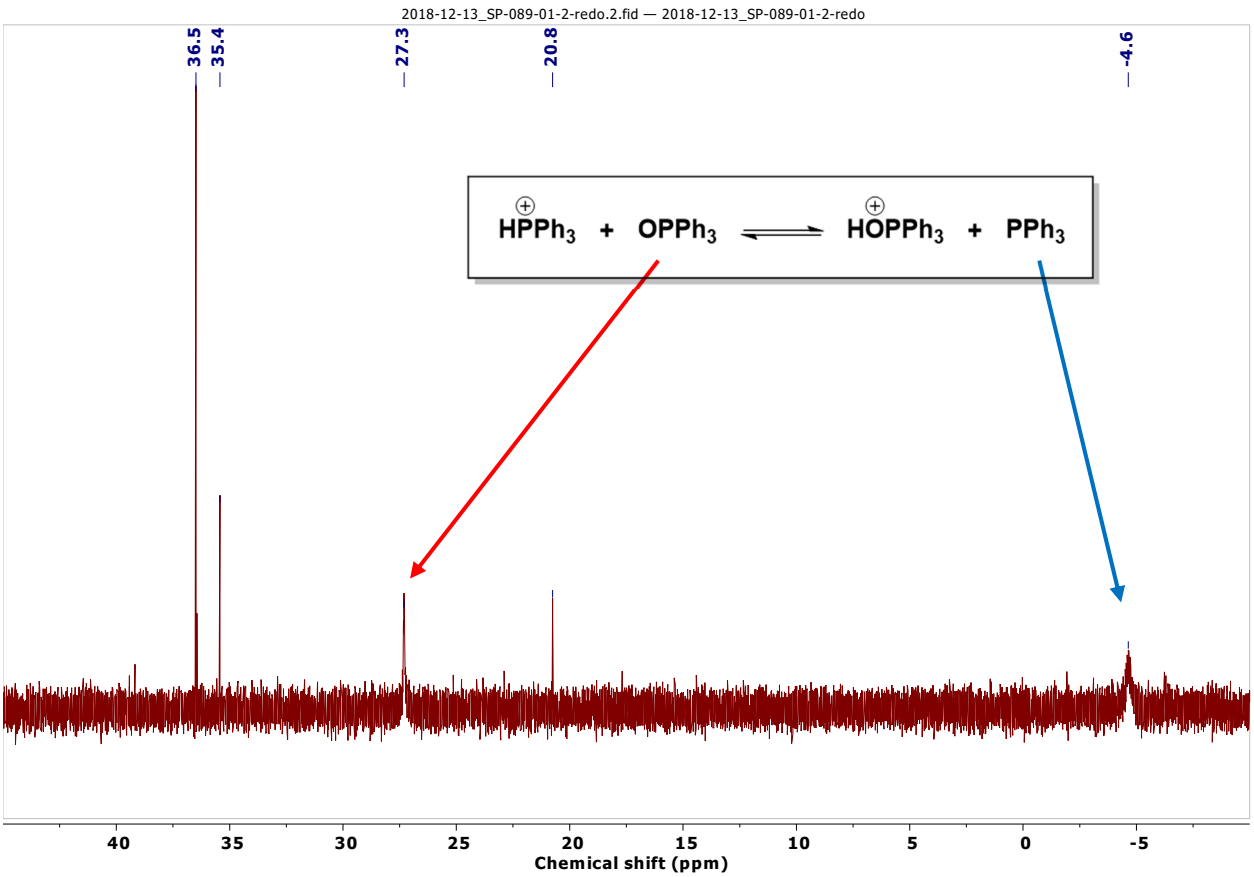

Figure S9. Portion of the ^{31}P NMR spectrum that shows broadening and downfield shift of the peaks corresponding to $OPPh_3$ and PPh_3. Inset shows the equilibrium attributable to this observation.

EPR Analysis

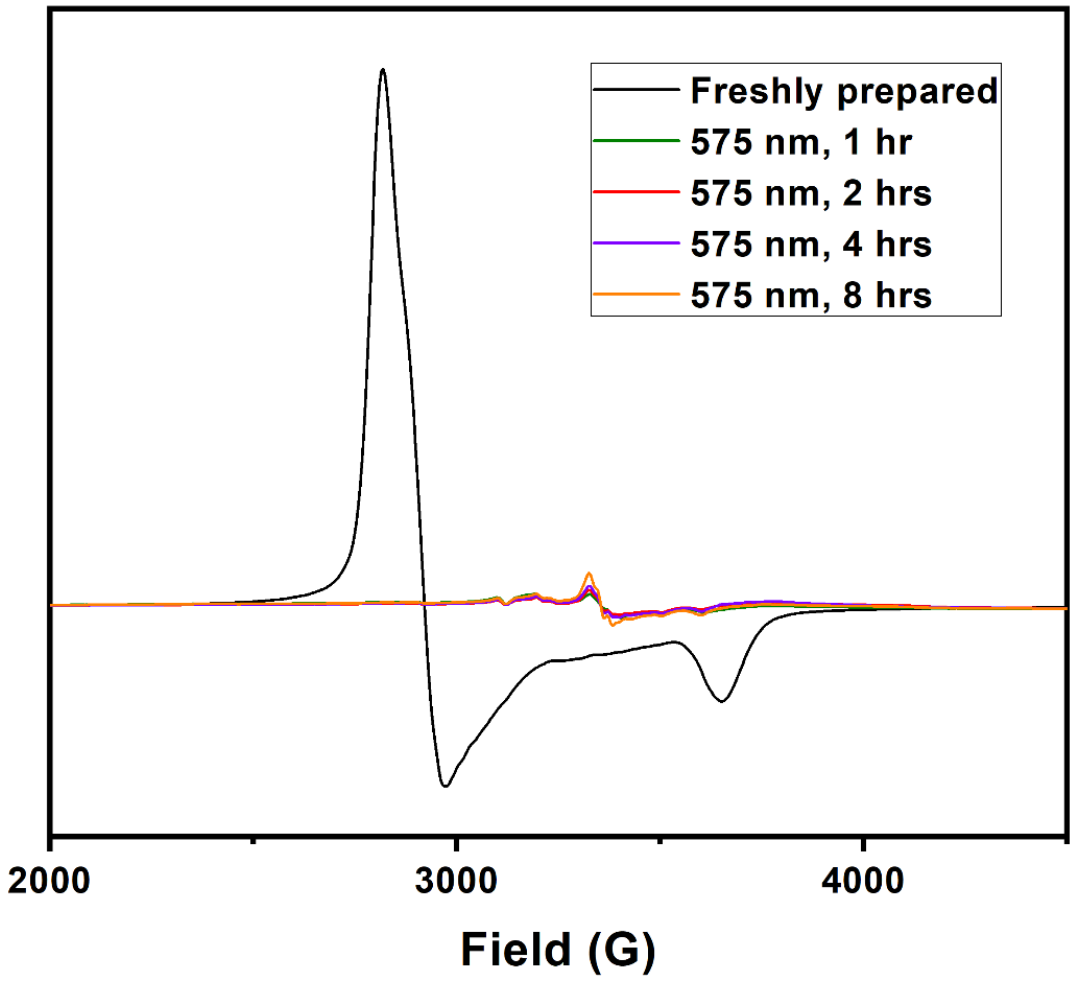

Figure S10. Visible light photolysis of **3′** (6.3 mM) at -196 °C monitored by EPR collected at 20 K.

Double integration of 3′

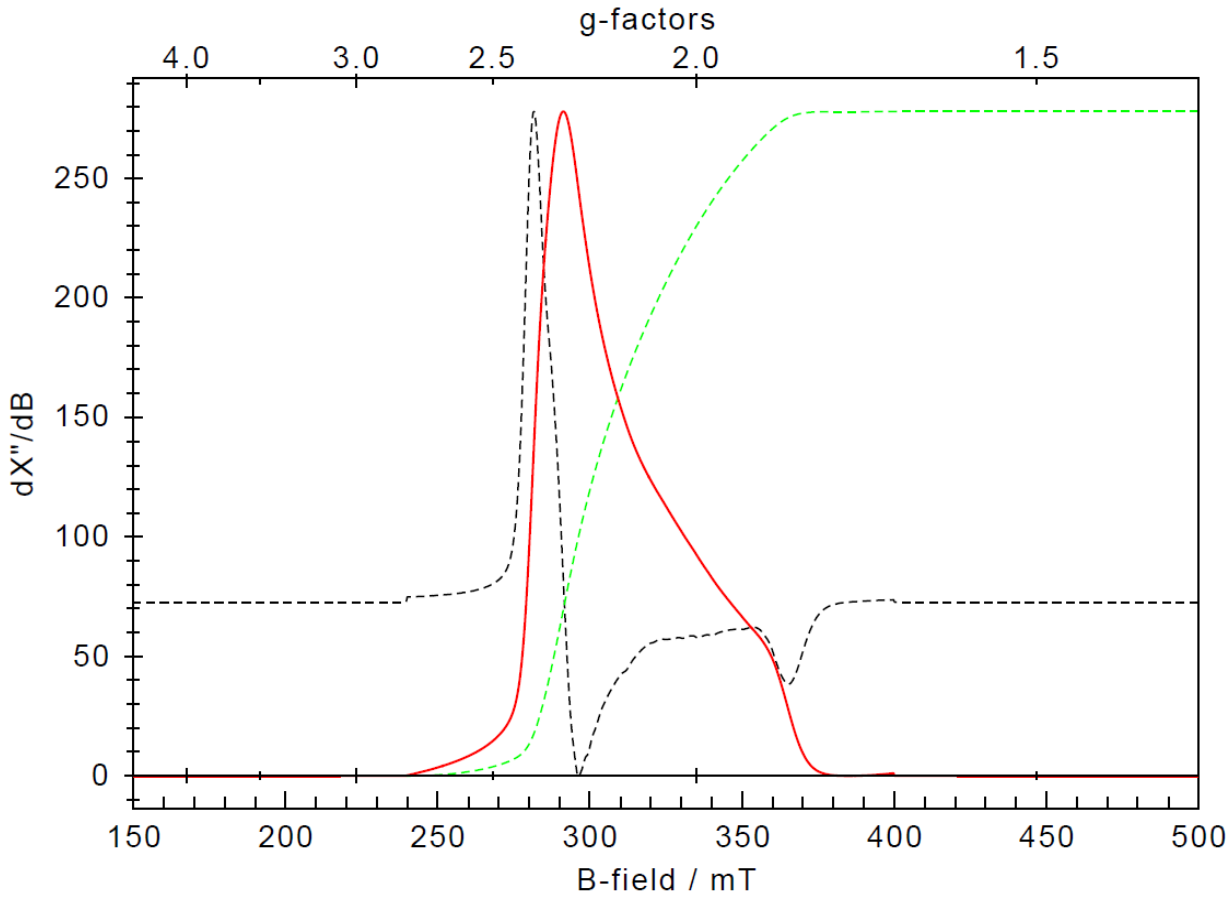

9.38004 GHz	m.w.-freq.
1.26 mW	m.w.-power
63.10	receiver gain
0.02 s	time constant
12.00 G	mod. amplitude
100.00 MHz	mod. frequency
0.00 deg	mod. phase
1.00 st	harmonic
3250.00 G	center field
3500.00 G	sweep
20.48 ms	ADC conv. time
8.00	number scans
1024.00 ch	nchan
0.00	ncurve

double integral: 0.12017E+05

Double integration of the product spectrum (2 hrs photolysis)

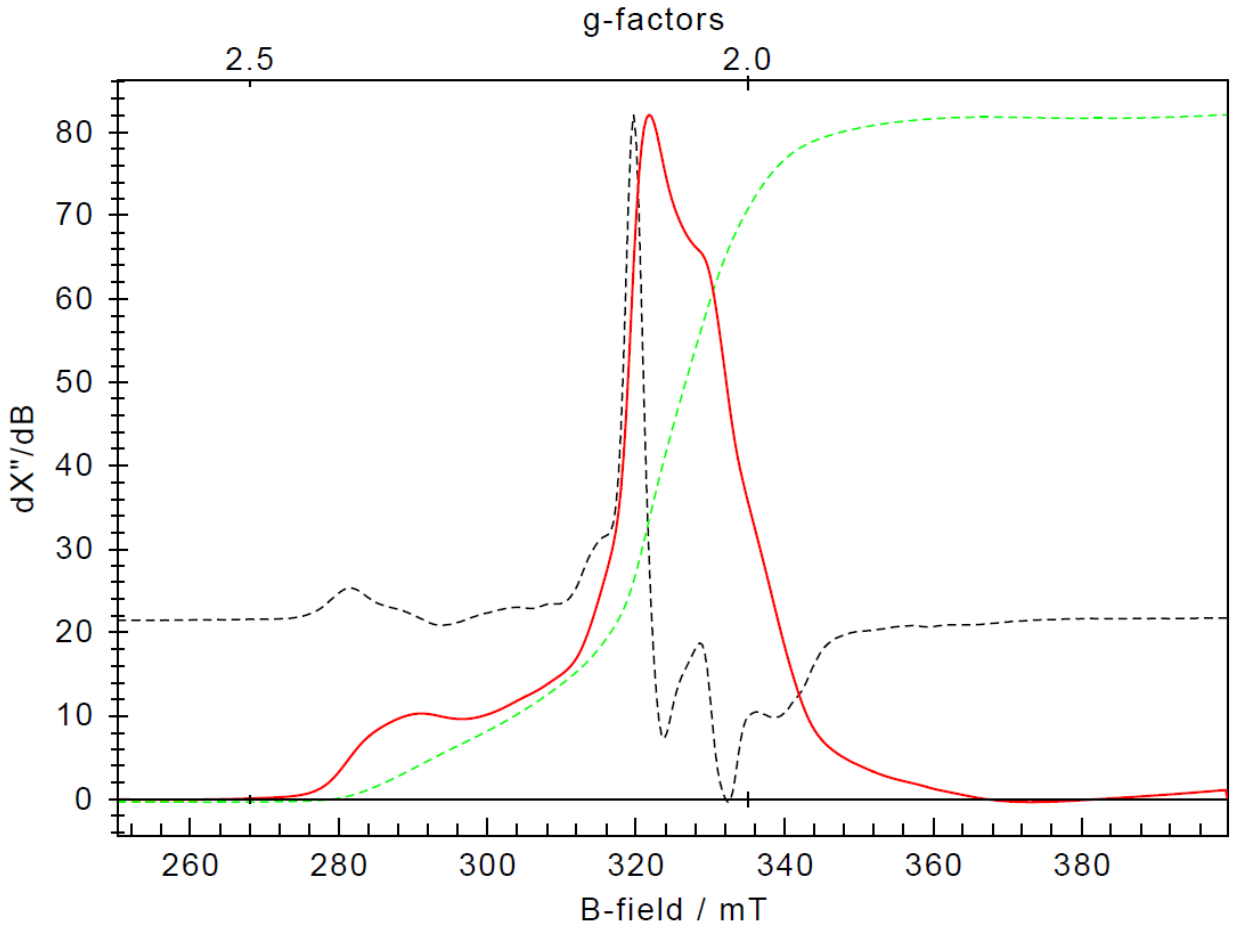

9.38015 GHz	m.w.-freq.
1.26 mW	m.w.-power
63.10	receiver gain
0.02 s	time constant
12.00 G	mod. amplitude
100.00 MHz	mod. frequency
0.00 deg	mod. phase
1.00 st	harmonic
3250.00 G	center field
1495.12 G	sweep
20.48 ms	ADC conv. time
8.00	number scans
438.00 ch	nchan
0.00	ncurve

double integral: 0.18176E+04

Simulation of the product spectrum (2 hrs photolysis)

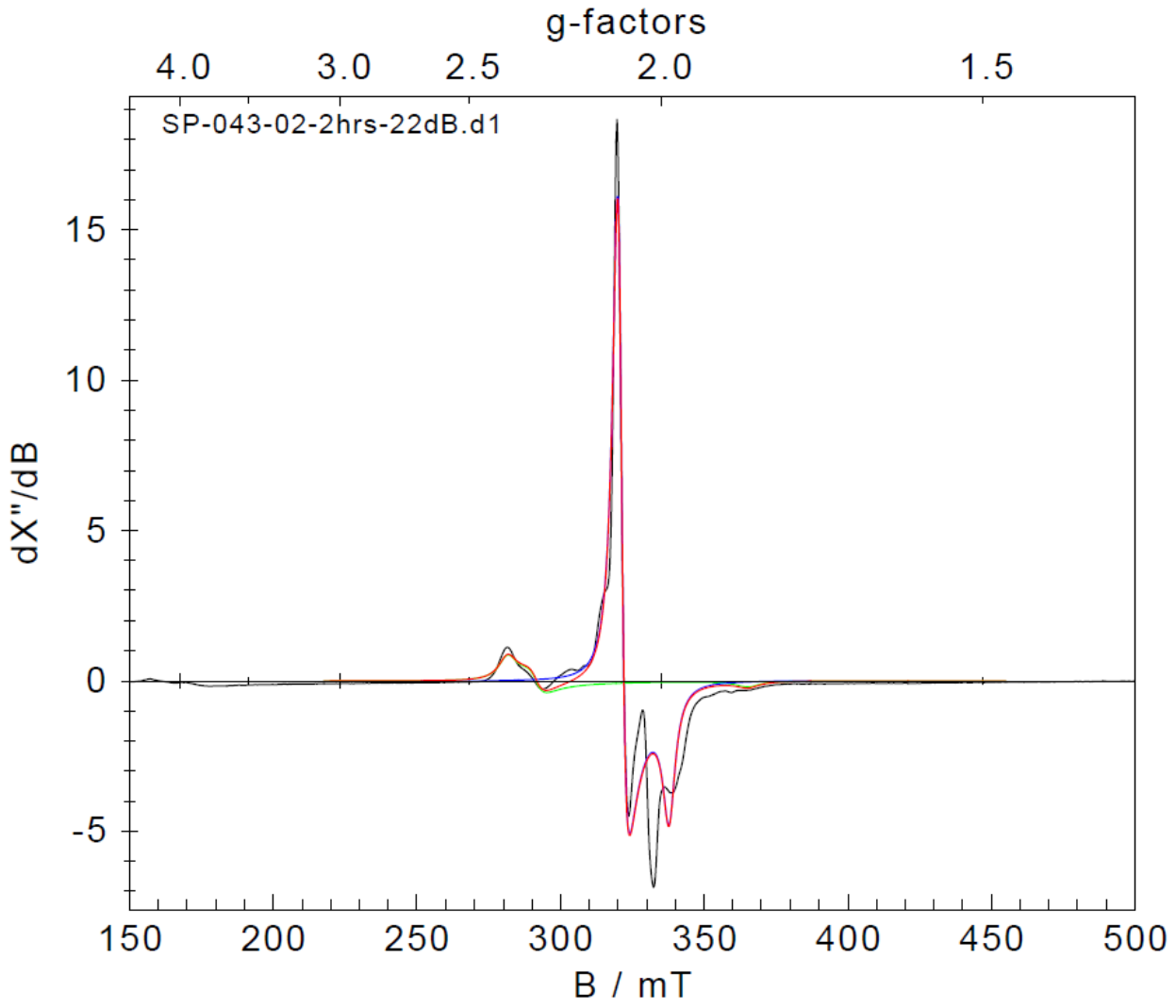

Total Int.(sim.): 0.3999E+03 B_Int.: 0.1556E+04 fsum: 0.3002E+03

1-	AMPL	0.7085E+00	1	2-	AMPL	0.1837E+01	1
1	gx	2.3803	0	1	gx	2.0899	1
2	gy	2.2985	0	2	gy	2.0900	1
3	gz	1.8348	0	3	gz	1.9838	1
4	W_f	5.1000	0	4	W_f	2.9677	1
5	Wx	0.0000	0	5	Wx	0.0000	0
6	Wy	0.0000	0	6	Wy	0.0000	0
7	Wz	0.0000	0	7	Wz	0.0000	0
8	V_x	0.0000	0	8	V_x	0.0000	0
9	V_y	0.0000	0	9	V_y	0.0000	0
10	V_z	0.0000	0	10	V_z	0.0000	0
Intens.:		0.1113E+03		Intens.:		0.2886E+03	
[%]:		27.8		[%]:		72.2	
S_Integ:		0.4851E+03		S_Integ:		0.1186E+04	
B_Integ:		0.4517E+03		B_Integ:		0.1104E+04	

units D/J: cm-1; Ai/wf/c1/c2: 10^-4cm-1; widths Wi: mT

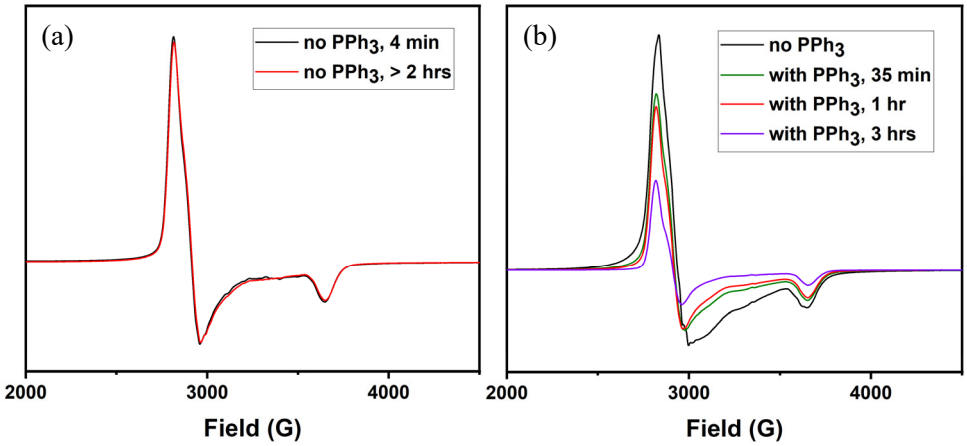

Figure S11. (a) Minimal decomposition of **3′** without PPh_3. (b) Decomposition of **3** in the presence of 1 equivalent of PPh_3.

Computational Methods

Computations were performed using the Orca software package version 4.1.1.[8] For all calculations, the def2-SVP basis set was used for all atoms except for the Ru atom, for which the def2-TZVPP basis set was applied.[9] Dispersion correction (D3)[10,11] and the relativistic approximation (ZORA) were used as well.

Geometry optimizations and frequency calculations were conducted with the BP86 functional along with the RI approximation and the SARC/J auxiliary basis set.[12]

The geometry optimizations for the $[(Py_5Me_2)Ru^{II}(N_3)]^+$ (**2**) and $[(Py_5Me_2)Ru^{III}(N_3)]^{2+}$ (**3**) cations were conducted with the crystal structures as inputs.[1] The crystal structure of $[(14\text{-TMC})Ru^{III}(N_3)_2]^+$ (**1**) is not reported, so its closest structural analogue $[(14\text{-TMC})Ru^{II}(MeCN)(N_3)]^+$ was used as the starting point for the geometry optimization with the carbon atoms in the acetonitrile ligand replaced with nitrogen atoms.

Transition state searches for the azide-to-nitride transformation of **3** and PPh_3 coordination to **3** were conducted with the aid of relaxed surfaced scans with the N–N bond distance being scanned from 1.0 Å to 4.0 Å or the P–N bond distance being scanned from 4.0 Å to 1.0 Å in ~0.05 Å increments with the DFT-optimized geometries used as inputs. For the relaxed surfaced scans, convergence was aided with the SlowConv keyword and the tolerance was readjusted with TolE 1e-7 and TolErr 1e-6. The structures at the local energy maxima along these surfaces were subsequently used as inputs for transition state optimization. Frequency calculations were conducted on all optimized transition state geometries to confirm the existence of a single imaginary vibrational frequency. Inspection of these imaginary modes confirmed that the computed transition states connect two distinct intermediates along the reaction coordinate.

Initial input geometries for the proposed nitrido compounds were attained by eliminating the two distal nitrogen atoms in the azide ligand from the benchmark crystal structures mentioned above. These structures were then subjected to geometry optimization.

Single point calculations for MO diagrams were conducted using the B3LYP functional[13] along with the RIJCOSX approximation and the SARC/J and def2-SVP/C auxiliary basis sets.[14]

Single point calculations for reaction energy profiles and Löwdin spin populations were conducted with the ωB97X-D3 functional[15,16] along with the RIJONX approximation and the SARC/J auxiliary basis set. Solvation effects were modeled using CPCM(acetone) for all the $(Py_5Me_2)Ru$ compounds and CPCM(acetonitrile) for all the (14-TMC)Ru compounds.

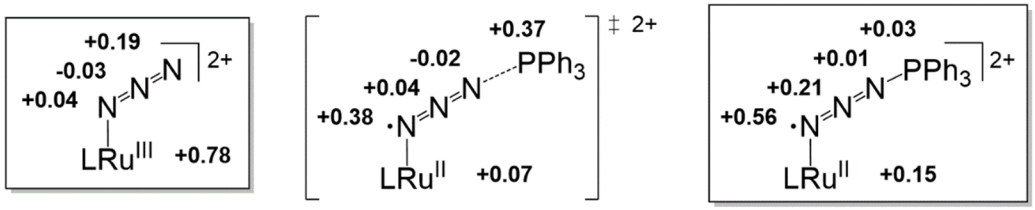

Figure S12. Löwdin spin populations of **3**, the transition state for coordination of PPh_3 to **3**, and the [Ru–N=N=N–PPh_3] intermediate.

Crystallographic Data

The structure for compound **3** • CH_3COCH_3 was processed as a two-component non-merohedral twin with a 20.3(2)% second component contribution. The twin components are related by a 179.6° rotation about the reciprocal axis [0 0 1]. The asymmetric unit consists of two $[(Py_5Me_2)Ru^{III}(N_3)]^{2+}$ cations, four hexafluorophosphate counteranions and two acetone molecules. The O1-acetone is disordered over two positions with a major component contribution of 81(6)%. The disordered atoms were refined with similarity restraints.

For $[(Py_5Me_2)Ru^{II}(Cl)](SbCl_6)_{0.70}(SbCl_4)_{0.30}$ • 2 CH_3COCH_3, the asymmetric unit consists of one half of a $[(Py_5Me_2)Ru^{II}(Cl)]^+$ cation, one half of a disordered antimonate anion that is 69.5% in the $SbCl_6^-$ form and 30.5% in the $SbCl_4^-$ form, one half of O1-acetone and one half of a disordered O2-acetone. The ruthenium complex, antimonate anion and acetone molecules all reside on a crystallographic mirror plane. The disordered atoms were refined with similarity restraints and constraints.

The asymmetric unit of $[(Py_5Me_2)Ru^{II}(PO_2F_2)](PO_2F_2)_{0.84}(PF_6)_{0.16}$ • 0.5 CH_3COCH_3 consists of two $[(Py_5Me_2)Ru^{II}(PO_2F_2)]^+$ cations, two phosphorus-containing counteranions partially in $PO_2F_2^-$ form and partially in PF_6^- form, and one acetone molecule. The $PO_2F_2^-$ ligand is disordered over two positions in each $[(Py_5Me_2)Ru^{II}(PO_2F_2)]^+$ cation, with a major component contribution of 60(2)% and 61(1)%, respectively. The $PO_2F_2^-$ counteranion is disordered over three positions with occupancies of 66.9(3)%, 59.8(3)% and 40.7(3)%, respectively. The PF_6^- counteranion is disordered over two positions with occupancies of 37.4(3)% and 27.8(3)%, respectively. The PF_6^- counteranion resides on a crystallographic inversion center, and only a half of it is present in the asymmetric unit. The acetone molecule is disordered over four positions with occupancies of 38.7(3)%, 26.1(3)%, 22.6(3)% and 12.7(3)%, respectively. The disordered atoms were refined with similarity restraints and constraints. A CSD survey was conducted to input restraints of 1.465 Å for P–O bond lengths and 1.527 Å for P–F bond lengths in the disordered $PO_2F_2^-$ counteranions. The acetone molecules were modeled using an idealized geometry.[17]

Compound	$[(Py_5Me_2)Ru^{III}(N_3)](PF_6)_2$ (**3**) • CH_3COCH_3	$[(Py_5Me_2)Ru^{II}(CH_3COCH_3)](PF_6)_2$ (**4**) • 2 CH_3COCH_3
Empirical formula	$C_{32}H_{31}F_{12}N_8OP_2Ru$	$C_{38}H_{43}F_{12}N_5O_3P_2Ru$
Formula weight	934.66	1008.78
Temperature/K	100.0	99.98
Crystal system	triclinic	triclinic
Space group	$P\bar{1}$	$P\bar{1}$
a/Å	15.546(4)	12.725(4)
b/Å	15.734(2)	12.889(4)
c/Å	16.911(2)	15.603(5)
α/°	99.81(1)	113.14(1)
β/°	116.88(1)	91.77(2)
γ/°	96.32(1)	117.69(1)
Volume/$Å^3$	3552(1)	2010(1)
Z	4	2
$\rho_{calc}g/cm^3$	1.748	1.666
μ/mm^{-1}	0.637	0.571
F(000)	1876.0	1024.0
Crystal size/mm^3	0.213 × 0.033 × 0.017	0.098 × 0.091 × 0.05
Radiation	MoKα (λ = 0.71073)	MoKα (λ = 0.71073)
2Θ range for data collection/°	2.688 to 52.97	2.942 to 56.672
Index ranges	$-19 \le h \le 16$, $-19 \le k \le 19$, $0 \le l \le 21$	$-16 \le h \le 16$, $-17 \le k \le 17$, $-20 \le l \le 20$
Reflections collected	14615	50307
Independent reflections	14615 [R_{int} = 0.1296, R_{sigma} = 0.1386]	9994 [R_{int} = 0.0410, R_{sigma} = 0.0383]
Data/restraints/parameters	14615/46/1032	9994/7/558
Goodness-of-fit on F^2	1.043	1.127
Final R indexes [I>=2σ (I)]	R_1 = 0.0667, wR_2 = 0.1234	R_1 = 0.0333, wR_2 = 0.0896
Final R indexes [all data]	R_1 = 0.1368, wR_2 = 0.1499	R_1 = 0.0436, wR_2 = 0.0921
Largest diff. peak/hole / e $Å^{-3}$	1.18/-1.13	0.69/-0.69

$R_1 = \Sigma||F_{obs}|-|F_{calc}|| / \Sigma|F_{obs}|$ and $wR_2 = [\Sigma w[F_{obs}^2-F_{calc}^2]^2 / \Sigma w[F_{obs}^2]^2]^{1/2}$

$w = 1 / [\ \sigma^2(F_{obs}^2) + (aP)^2 + bP\ ]$, where P is $[\ 2F_{calc}^2 + Max(F_{obs}^2,0)\ ] / 3$

$GoF = [[\Sigma w[F_{obs}^2-F_{calc}^2]^2] / (n-p)]^{1/2}$ (n = number of measured intensities, p = number of parameters)

Compound	$[(Py_5Me_2)Ru^{II}(Cl)](SbCl_6)_{0.70}(SbCl_4)_{0.30} \cdot 2\ CH_3COCH_3$	$[(Py_5Me_2)Ru^{II}(Cl)](PF_6) \cdot CH_3COCH_3$	$[(Py_5Me_2)Ru^{II}(PO_2F_2)](PO_2F_2)_{0.84}(PF_6)_{0.16} \cdot 0.5\ CH_3COCH_3$
Empirical formula	$C_{35}H_{37}Cl_{6.39}N_5O_2RuSb$	$C_{32}H_{31}ClF_6N_5OPRu$	$C_{30.5}H_{28}F_{4.65}N_5O_{4.17}P_2Ru$
Formula weight	1009.04	783.11	782.78
Temperature/K	100.0	99.99	100.0
Crystal system	orthorhombic	orthorhombic	triclinic
Space group	*Pnma*	$Pmc2_1$	$P\bar{1}$
a/Å	23.348(7)	10.366(3)	11.390(4)
b/Å	13.355(4)	8.964(3)	16.353(5)
c/Å	12.292(4)	17.126(6)	20.162(6)
α/°	90	90	99.44(1)
β/°	90	90	94.92(1)
γ/°	90	90	109.59(2)
Volume/$Å^3$	3833(2)	1591.3(9)	3450(2)
Z	4	2	4
$\rho_{calc}g/cm^3$	1.749	1.634	1.507
μ/mm^{-1}	1.584	0.698	0.615
F(000)	2007.0	792.0	1581.0
Crystal size/mm^3	0.085 × 0.072 × 0.061	0.083 × 0.06 × 0.016	0.089 × 0.055 × 0.024
Radiation	MoKα (λ = 0.71073)	MoKα (λ = 0.71073)	MoKα (λ = 0.71073)
2Θ range for data collection/°	3.488 to 54.3	3.93 to 54.26	2.072 to 52.834
Index ranges	$-29 \le h \le 29, -17 \le k \le 17, -15 \le l \le 15$	$-13 \le h \le 13, -11 \le k \le 11, -21 \le l \le 21$	$-14 \le h \le 14, -20 \le k \le 20, -25 \le l \le 25$
Reflections collected	70231	29870	74964
Independent reflections	4428 [R_{int} = 0.0485, R_{sigma} = 0.0183]	3704 [R_{int} = 0.0451, R_{sigma} = 0.0253]	14156 [R_{int} = 0.1337, R_{sigma} = 0.1126]
Data/restraints /parameters	4428/67/339	3704/35/255	14156/366/1084
Goodness-of-fit on F^2	1.159	1.064	1.043
Final R indexes [I>=2σ (I)]	R_1 = 0.0410, wR_2 = 0.0919	R_1 = 0.0237, wR_2 = 0.0575	R_1 = 0.0882, wR_2 = 0.2513
Final R indexes [all data]	R_1 = 0.0480, wR_2 = 0.0955	R_1 = 0.0252, wR_2 = 0.0584	R_1 = 0.1633, wR_2 = 0.3014
Largest diff. peak/hole / e $Å^{-3}$	1.29/-1.29	0.72/-0.34	1.81/-0.85
Flack parameter	-	0.005(12)	-

$R_1 = \Sigma||F_{obs}|-|F_{calc}|| / \Sigma|F_{obs}|$ and $wR_2 = [\Sigma w[F_{obs}^2-F_{calc}^2]^2 / \Sigma w[F_{obs}^2]^2]^{1/2}$

$w = 1 / [\ \sigma^2(F_{obs}^2) + (aP)^2 + bP\ ]$, where P is $[\ 2F_{calc}^2 + Max(F_{obs}^2,0)\ ] / 3$

$GoF = [[\Sigma w[F_{obs}^2-F_{calc}^2]^2] / (n-p)]^{1/2}$ (n = number of measured intensities, p = number of parameters)

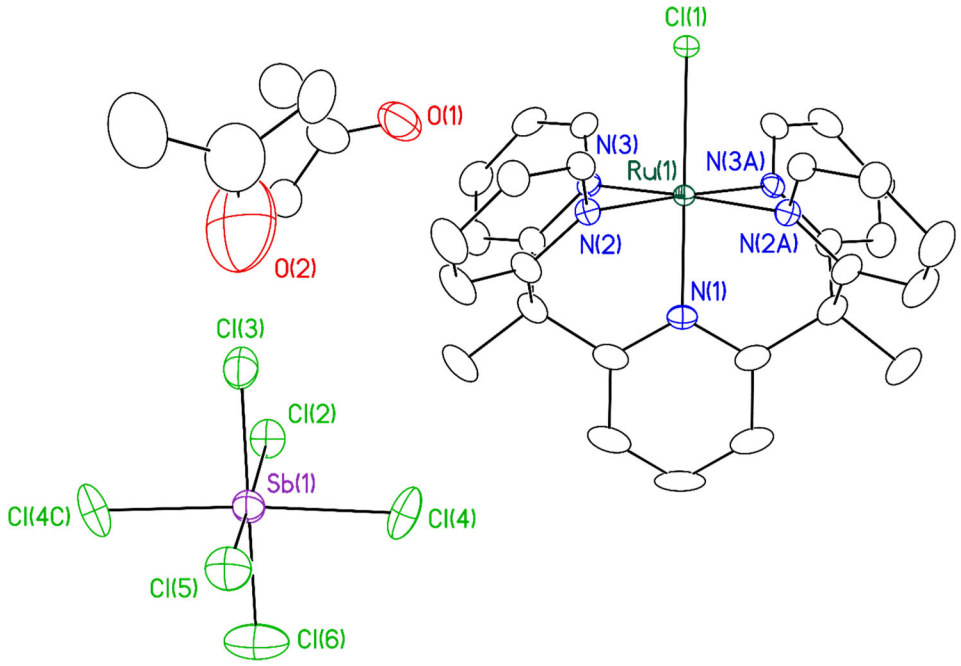

Figure S13. A molecular drawing of $[(Py_5Me_2)Ru^{II}(Cl)](SbCl_6)_{0.70}(SbCl_4)_{0.30} \bullet 2\ CH_3COCH_3$ shown with 50% probability ellipsoids. Only the major component (the $SbCl_6^-$ form) of the disordered antimonate anion and only the major component of the disordered O2-acetone are shown. All H atoms are omitted.

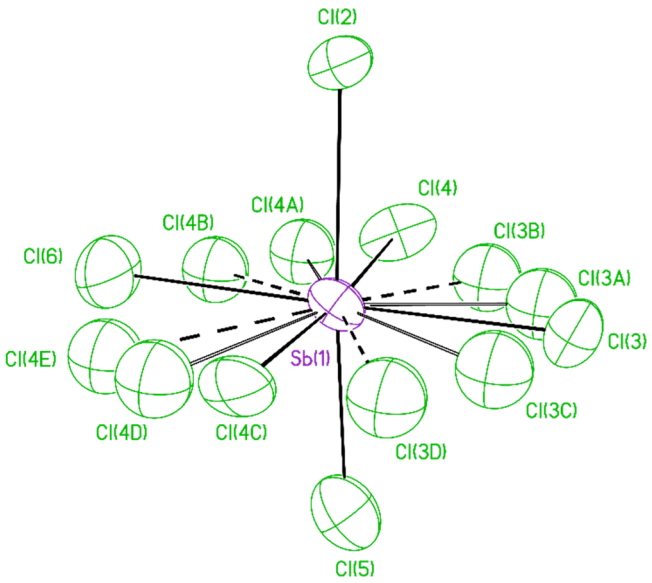

Figure S14. The antimonate anion in $[(Py_5Me_2)Ru^{II}(Cl)](SbCl_6)_{0.70}(SbCl_4)_{0.30} \bullet 2\ CH_3COCH_3$ shown with 50% probability ellipsoids. All disordered atoms are shown.

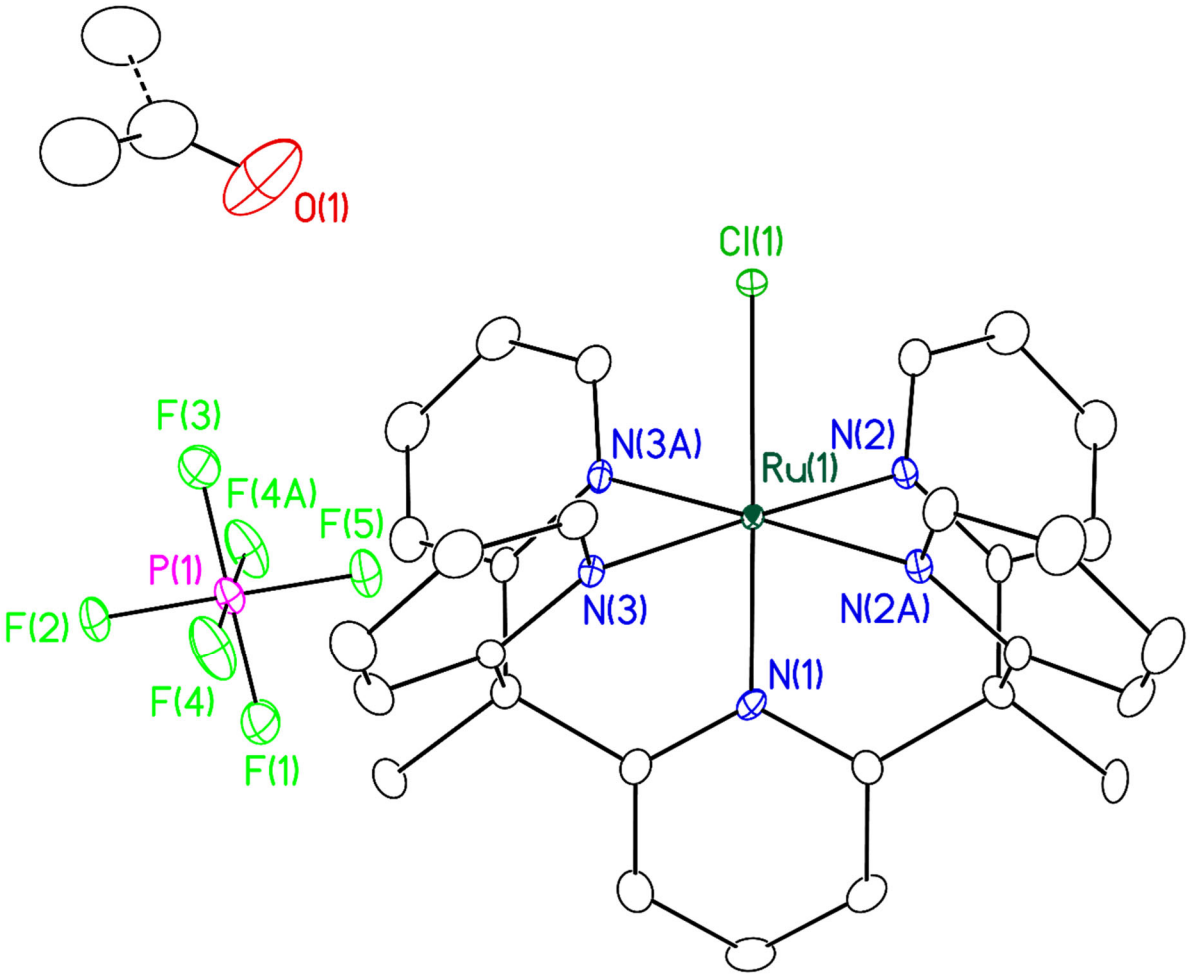

Figure S15. A molecular drawing of $[(Py_5Me_2)Ru^{II}(Cl)](PF_6) \bullet CH_3COCH_3$ shown with 50% probability ellipsoids. Only one out of two components (with equal occupancies) of the disordered acetone is shown. All H atoms are omitted.

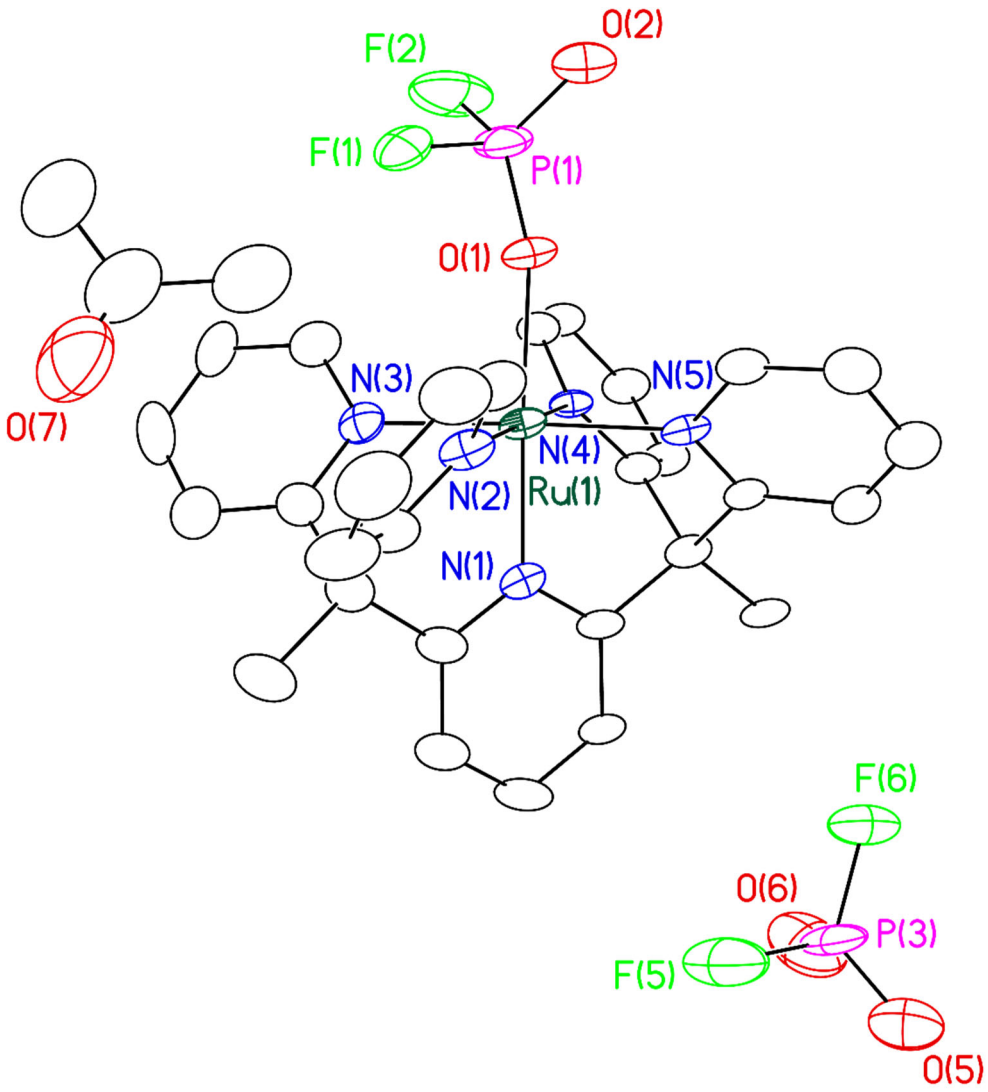

Figure S16. A molecular drawing of $[(Py_5Me_2)Ru^{II}(PO_2F_2)](PO_2F_2)_{0.84}(PF_6)_{0.16} \bullet 0.5\ CH_3COCH_3$ shown with 30% probability ellipsoids. Only the major component of the disordered $PO_2F_2^-$ ligand, disordered counteranion and disordered acetone is shown. All H atoms are omitted.

Calculation of Kinetic Parameters

The absorbance at λ = 551 nm was monitored for the light-driven decomposition of **3** in dry acetone at -78 °C. A nonlinear least-squares regression analysis was conducted for the equation $[\mathbf{3}] = e^{-kt}\,[\mathbf{3}]_0$ using the MATLAB software with the lsqcurvefit and nlparci commands.[18] The analysis converged to a rate constant k = 0.327(4) min^{-1} (5.45(6) × 10^{-3} s^{-1}) for the first-order decay process.

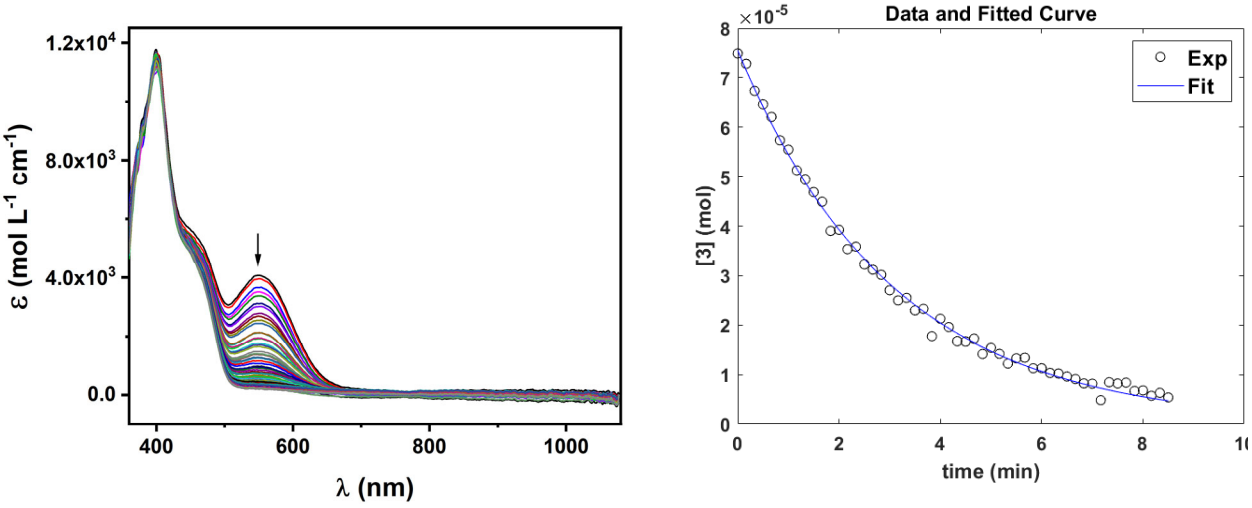

Figure S17. UV/vis traces obtained for the decomposition of **3** obtained at 10 second intervals (left), and a MATLAB fit to the absorbance values at λ = 551 nm (right).

Molecular Orbital Diagrams

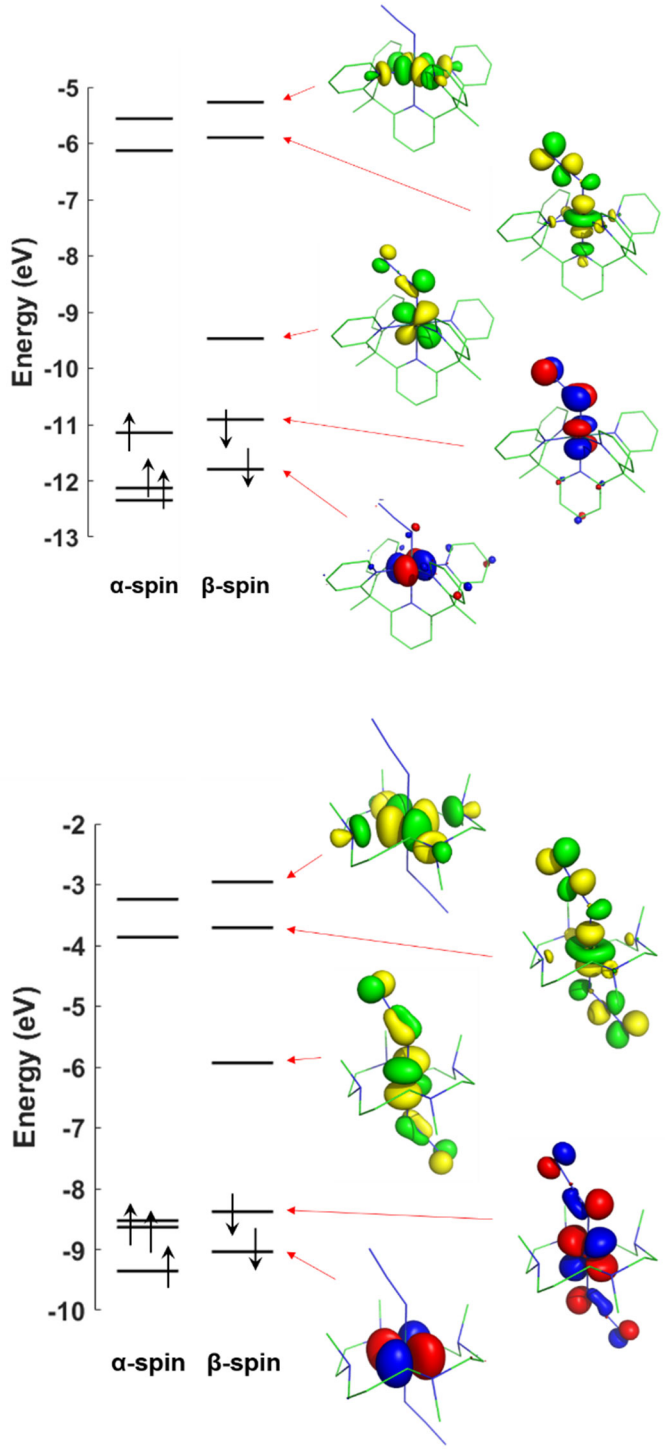

Figure S18. Calculated 4d orbital manifold for complexes **1** (below) and **3** (above). The red/blue colors indicate occupied while green/yellow colors indicate unoccupied beta spin MO's.

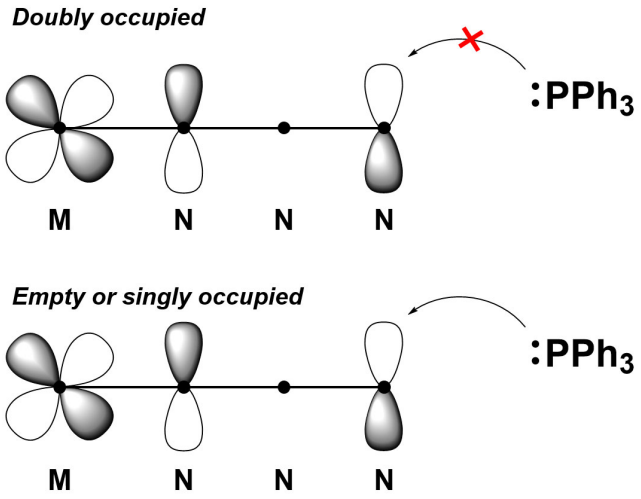

Figure S19. Strategy employed in this work for switching on metallo-Staudinger reactivity.

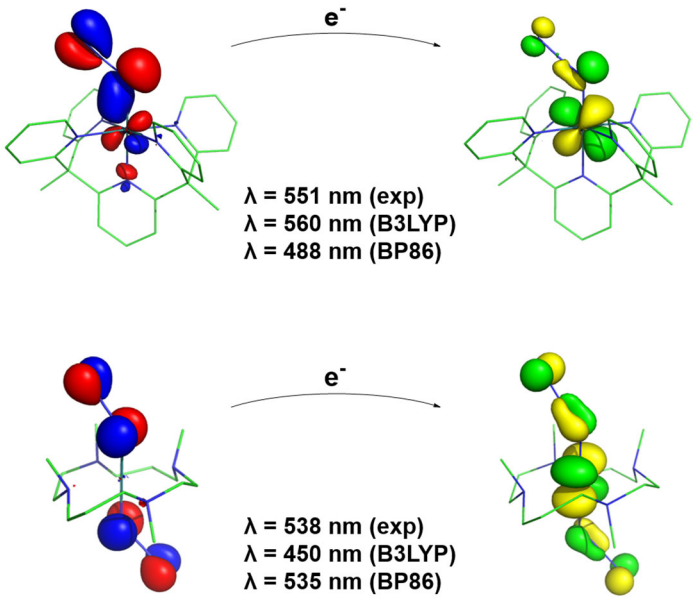

Figure S20. Electronic transitions that result from irradiation of **1** (below) and **3** (above), respectively. Wavelength values are obtained either from the experimental UV/vis spectrum[19] or from a TD-DFT calculation using the functional in the parenthesis; the MO depictions are derived from B3LYP single point calculations.

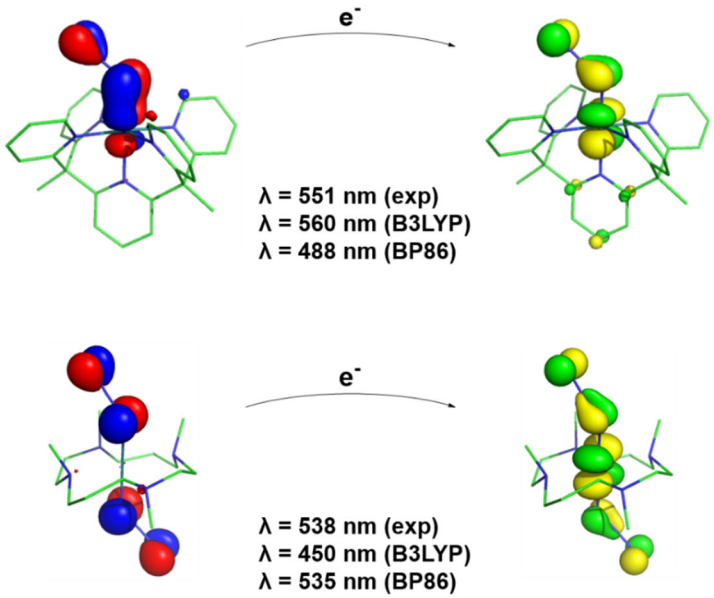

Figure S21. Electronic transitions that result from irradiation of **1** (below) and **3** (above), respectively. Wavelength values are obtained either from the experimental UV/vis spectrum[19] or from a TD-DFT calculation using the functional in the parenthesis; the MO depictions are derived from BP86 single point calculations.

References

1 S. V. Park and J. F. Berry, *Dalton Trans.*, 2017, **46**, 9118–9125.

2 T. Nishinaga, *Organic Redox Systems*, John Wiley & Sons, Inc., 2016.

3 R. K. Harris, E. D. Becker, S. M. Cabral de Menezes, R. Goodfellow and P. Granger, *Pure Appl. Chem.*, 2001, **73**, 1795–1818.

4 R. K. Harris, E. D. Becker, S. M. Cabral de Menezes, P. Granger, R. E Hoffman and K. W. Zilm, *Pure Appl. Chem.*, 2008, **80**, 59–84.

5 W. J. Transue, J. Yang, M. Nava, I. V. Sergeyev, T. J. Barnum, M. C. McCarthy and C. C. Cummins, *J. Am. Chem. Soc.*, 2018, **140**, 17985–17991.

6 S. Ohzu, T. Ishizuka, H. Kotani and T. Kojima, *Chem. Commun.*, 2014, **50**, 15018–15021.

7 M. Althaus, C. Bonaccorsi, A. Mezzetti and F. Santoro, *Organometallics*, 2006, **25**, 3108–3110.

8 F. Neese, *Wiley Interdiscip. Rev. Comput. Mol. Sci.*, 2012, **2**, 73–78.

9 F. Weigend and R. Ahlrichs, *Phys. Chem. Chem. Phys.*, 2005, **7**, 3297–3305.

10 S. Grimme, J. Antony, S. Ehrlich and H. Krieg, *J. Chem. Phys.*, 2010, **132**, 154104.

11 S. Grimme, S. Ehrlich and L. Goerigk, *J. Comput. Chem.*, 2011, **32**, 1456–1465.

12 F. Weigend, *Phys. Chem. Chem. Phys.*, 2006, **8**, 1057–1065.

13 P. J. Stephens, F. J. Devlin, C. F. Chabalowski and M. J. Frisch, *J. Phys. Chem.*, 1994, **98**, 11623–11627.

14 A. Hellweg, C. Hättig, S. Höfener and W. Klopper, *Theor. Chem. Acc.*, 2007, **117**, 587–597.

15 J. Da Chai and M. Head-Gordon, *J. Chem. Phys.*, 2008, **128**, 084106.

16 Y. S. Lin, G. De Li, S. P. Mao and J. Da Chai, *J. Chem. Theory Comput.*, 2013, **9**, 263–272.

17 I. A. Guzei, *J. Appl. Crystallogr.*, 2014, **47**, 806–809.

18 C. L. Perrin, *J. Chem. Educ.*, 2017, **94**, 669–672.

19 C. M. Ho, H. C. Leung, S. Wu, K. H. Low, Z. Lin and C. M. Che, *Eur. J. Inorg. Chem.*, 2012, 151–159.